NANO · MICRO small
www.small-journal.com

Check for updates

Quantum Nature of Charge Transport in Inkjet-Printed Graphene Revealed in High Magnetic Fields up to 60T

Nathan D. Cottam, Feiran Wang, Jonathan S. Austin, Christopher J. Tuck, Richard Hague, Mark Fromhold, Walter Escoffier, Michel Goiran, Mathieu Pierre, Oleg Makarovsky, and Lyudmila Turyanska**

Inkjet-printing of graphene, iGr, provides an alternative route for the fabrication of highly conductive and flexible graphene films for use in devices. However, the contribution of quantum phenomena associated with 2D single layer graphene, SLG, to the charge transport in iGr is yet to be explored. Here, the first magneto-transport study of iGr in high magnetic fields up to 60 T is presented. The observed quantum phenomena, such as weak localization and negative magnetoresistance, are strongly affected by the thickness of the iGr film and can be explained by a combination of intra- and inter-flake classical and quantum charge transport. The quantum nature of carrier transport in iGr is revealed using temperature, electric field, and magnetic field dependences of the iGr conductivity. These results are relevant for the exploitation of inkjet deposition of graphene, which is of particular interest for additive manufacturing and 3D printing of flexible and wearable electronics. It is shown that printed nanostructures enable ensemble averaging of quantum interference phenomena within a single device, thereby facilitating comparison between experiment and underlying statistical models of electron transport.

1. Introduction

Isolation of single layer graphene (SLG) triggered disruptive changes in the fundamental science of 2D materials and device applications,[1,2] and enabled observation of novel quantum effects, such as the Quantum Hall Effect at temperatures as high as 300 K,[3] weak localization and antilocalization phenomena.[4–8] Pronounced quantum effects in SLG are attributed to its high carrier mobility[1,2] and linear Dirac cone-shaped dispersion, which lead to large energy gaps between the Landau levels that form in a quantizing magnetic field and enables control of both the carrier type and concentration in graphene field effect transistors (GFETs).[1,2,9]

Liquid exfoliation of graphene offers an alternative route for production of 2D materials,[10–12] which can be used to formulate inks for scalable deposition by drop-on-demand inkjet additive manufacturing.[13] In applied electric and magnetic fields, the inkjet deposited graphene (iGr) devices demonstrate behaviors qualitatively similar to typical SLG devices, such as minimum conductivity in the Dirac point, switching from *p*- to *n*-type conductivity with increasing applied gate voltage and minimum conductivity in zero magnetic field due to weak localization.[10,11] However, compared to SLG,[9] iGr typically has significantly lower carrier mobility of <100 cm^2/Vs,[10,11] which is attributed to the increased complexity of charge transport through the graphene network. Temperature-dependent studies of the iGr conductivity indicate carrier hopping mechanisms of charge transport,[11,14] with strong gate voltage dependence of FET conductivity even in thick (>100 nm) iGr films.[11] To date, quantum phenomena, such as the Quantum Hall Effect or Shubnikov-de Haas oscillations of magnetoresistance were not observed in iGr and the contribution of quantum transport to the properties of these printed films is yet to be probed.

In this letter we investigate the quantum and classical phenomena in iGr devices of different thickness, from a single droplet to multiple inkjet-printed layers in a wide range of temperatures (T = 1.8 to 400 K) and magnetic fields up to 60 T. We demonstrate that, under certain conditions, such as those achieved in the droplet samples, iGr behaves mostly as a

N. D. Cottam, M. Fromhold, O. Makarovsky
School of Physics and Astronomy
University of Nottingham
University Park
Nottingham NG7 2RD, UK
E-mail: Oleg.Makarovsky@nottingham.ac.uk
F. Wang, J. S. Austin, C. J. Tuck, R. Hague, L. Turyanska
Centre for Additive Manufacturing
Faculty of Engineering
University of Nottingham
Jubilee Campus, Nottingham NG8 1BB, UK
E-mail: Lyudmila.Turyanska@nottingham.ac.uk
W. Escoffier, M. Goiran, M. Pierre
INSA Toulouse
Université Paul Sabatier
Université de Toulouse
LNCMI UPR CNRS 3228, EMFL, 143 Avenue de Rangueil, Toulouse 31400, France

The ORCID identification number(s) for the author(s) of this article can be found under https://doi.org/10.1002/smll.202311416

© 2024 The Authors. Small published by Wiley-VCH GmbH. This is an open access article under the terms of the Creative Commons Attribution License, which permits use, distribution and reproduction in any medium, provided the original work is properly cited.

DOI: 10.1002/smll.202311416

16136829, 0, Downloaded from https://onlinelibrary.wiley.com/doi/10.1002/smll.202311416 by University Of Nottingham, Wiley Online Library on [05/03/2024]. See the Terms and Conditions (https://onlinelibrary.wiley.com/terms-and-conditions) on Wiley Online Library for rules of use; OA articles are governed by the applicable Creative Commons License

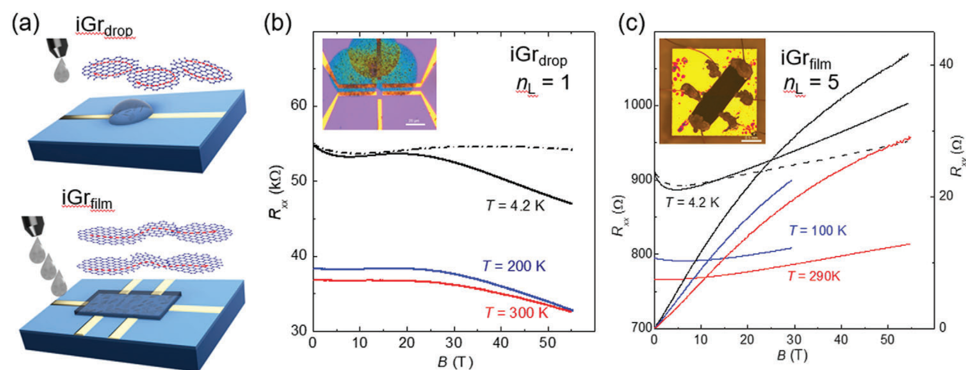

Figure 1. a) Sketch of the fabrication process of a single droplet (top) and printed layers film (bottom) iGr devices. b) High magnetic field ($B < 60$ T) longitudinal, R_{xx}, of a single droplet device at different temperatures in magnetic fields applied perpendicular (solid lines) and parallel (dashed lines) to the sample surface. Inset is an optical image of a droplet device. c) R_{xx}, (bold lines) and transverse, R_{xy}, (thin lines) for an iGr$_{film}$ device (shown in the inset (a)) in magnetic fields applied perpendicular (solid lines) and parallel (dashed lines) to the sample surface. Inset is an optical image of an iGr$_{film}$ device.

quantum material showing quantum effects of weak localization, negative magnetoresistance and temperature dependence of conductivity explained by a scaling model. To the best of our knowledge, this is the first report of negative magnetoresistance in graphene networks. We experimentally measure and explain quantum properties of iGr in the quantizing magnetic fields up to 60 T, revealing the contribution of quantum phenomena on charge transport through graphene networks, which could underpin the development of graphene-based devices and printed electronics.

2. Results and Discussion

2.1. Magnetic Field Studies of iGr Devices

To explore the charge transport phenomena, two sets of iGr devices were fabricated – individual droplets (iGr$_{drop}$) and films (iGr$_{film}$) created by printing a number of iGr layers $1 < n_L < 20$ (**Figure 1a**). The graphene ink contains individual graphene flakes with average size of ≈50 nm. All studied samples were deposited using inkjet printing and the same post-deposition treatment parameters were used. For multidrop devices, the individual drops were deposited consecutively at the same position; while for film devices each layer is printed with individual droplets overlapping by ≈50% (see Experimental Section for details).[13] The sheet resistance of these devices is independent of the device size, substrate type (e.g., Si/SiO_2, glass, Kapton) and contact material (Au and Ag contacts) (Section S1, Supporting Information). We note, that the size of individual flakes is significantly smaller than the size of a droplet (≈50 µm) and the distance between the electrical contacts. Hence for the film and the droplet devices, we measure the electrical properties of graphene flake networks. At high ($B < 60$ T) and low ($B < 16$ T) magnetic field, the magnetoresistance (MR) of a single droplet and film devices revealed significantly different behavior (**Figures 1** and **2**; Section S1, Supporting Information).

At low temperatures ($T < 200$ K), single droplet devices demonstrate a pronounced magnetoresistance (MR) dip in magnetic fields of $B < 10$ T applied perpendicular to the current flow followed by a local MR maximum at $B = 20$ T and a negative MR at $20\text{ T} < B < 60$ T. However, at high temperatures ($T > 200$ K) and low $B < 20$ T, MR becomes almost independent on the applied magnetic field (Figures 1b and 2a). With increasing B, strong negative MR is observed even at room temperature (Figure 1b). In the direction parallel to the magnetic field, negative MR is significantly reduced and MR dip becomes smaller and broader (dashed line in Figure 1b).

iGr$_{film}$ devices fabricated with the number of printed layers n_L = 1 to 20, revealed similar behavior to that of the droplets in low magnetic fields $B < 6$ T with a pronounced MR dip at $B \approx 5$

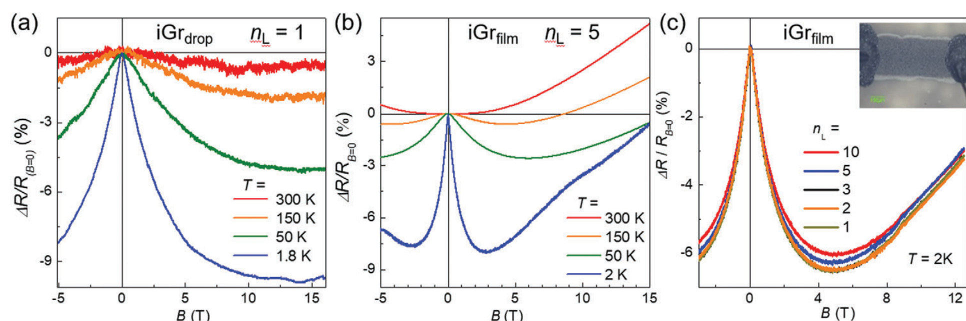

Figure 2. Low perpendicular magnetic field ($B < 16$T) longitudinal magnetoresistance ($\Delta R_{xx}/R_{xx}(B = 0)$) of a) iGr$_{drop}$ and b) iGr$_{film}$ with the number of printed layers, $n_L = 5$ at different temperatures. c) Magnetoresistance for iGr films with different number of layers printed on sapphire substrates at $T =$ 2K. Inset: Photograph of the iGr$_{film}$ device with $n_L = 3$ on a sapphire substrate.

 © 2024 The Authors. Small published by Wiley-VCH GmbH

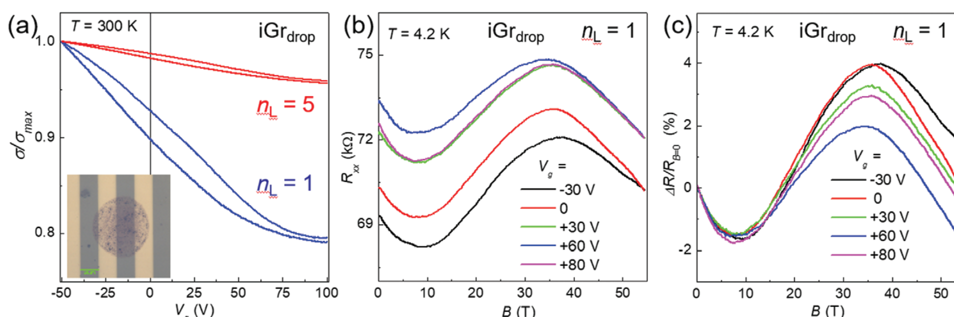

Figure 3. a) Normalised gate voltage effect on iGr conductivity measured on a single iGr droplet and 5 droplets devices at $B = 0$ and $T = 300$ K. Different lines of the same color correspond to different directions of gate voltage sweep. Insets: optical microscopy image of the single droplet (iGr_{drop}) device, scale bar 10 µm. Gate voltage effect on b) measured and c) relative magnetoresistance of a single droplet sample measured at the perpendicular magnetic field $B < 55$ T at $T = 4.2$ K.

T (Figures 1c and 2c). However, at $B > 6$ T a positive parabolic MR, typical for 3D semiconductors, is observed at $T > 100$ K (Figures 1c and 2b). Linear dependence of Hall voltage on B observed at $B < 10$ T, becomes sublinear at higher magnetic fields (Figure 1c). In parallel magnetic fields, the MR dip as well as positive MR becomes weaker in low ($B < 5$ T) and high B, respectively. From the linear fits of $R_{xy}(B)$ Hall effect in $B < 5$ T, we estimate Hall mobility of the film devices, $\mu_H = 13$ cm^2 V^{-1} s^{-1} at $T = 4$ K and 9 cm^2 V^{-1} s^{-1} at $T = 290$ K

Gate voltage dependences of normalized conductivity, $\sigma/\sigma_{max}(V_g)$ of single and 5 droplet iGr devices (**Figure** 3a), revealed ≈20% decrease of the conductivity at $V_g < 100$ V and a conductivity minimum at $V_g \approx 90$ V for a single droplet device. The observed $\sigma(V_g)$ dependences (Figure 3a) are similar to those reported for single layer CVD graphene GFETs with low $\mu < 1000$ cm^2 V^{-1} s^{-1}.[15,16] In contrast to droplet devices, the iGr_{film} devices on Si/SiO_2 substrates do not show any measurable $\sigma(V_g)$ dependence (Section S2, Supporting Information).

The $\sigma(V_g)$ for all droplet iGr devices is highly reproducible, however, with increasing number of droplets the effect of V_g on device conductivity becomes weaker (Figure 3a). We note that conductivity becomes independent of V_g in film devices (Section S2, Supporting Information). We do not observe a strong hysteresis of $\sigma(V_g)$ with forward and reversed V_g sweeps (Figure 3a), that is normally associated with the presence of organic residues.[17,12] From $\sigma(V_g)$ dependences, we estimate the field-effect mobility and carrier concentration of $\mu = 2.3$ cm^2 V^{-1} s^{-1} and $p = 7.7 \times 10^{12}$ cm^{-2} for the single droplet and $\mu = 9.4$ cm^2 V^{-1} s^{-1} and $p = 9.3 \times 10^{12}$ cm^{-2} for the 5 droplet devices, at $V_g = 0$ (Section S2, Supporting Information). At perpendicular magnetic fields $B < 20$ T, the relative MR, $\Delta R/R(B = 0)$ is independent of V_g, while an onset of negative MR is observed at $B > 30$ T is gate voltage-dependent (Figure 3b,c). Interestingly, relative $\Delta R/R_{B=0}$ MR at $B > 35$ T demonstrates the same slope for all the values of applied V_g (Figure 3c), suggesting that the same linear negative MR could be interpreted as a transport behavior, independent of the carrier density.

Temperature dependences of conductivity $\sigma(T)$ at $B = 0$ T revealed a significant difference between the droplet and film devices (**Figure** 4a–c). To explain this difference, we assume random ordering of the flakes into graphene networks and apply Variable Range Hopping (VRH) transport models[18–20] (Figure 4b):

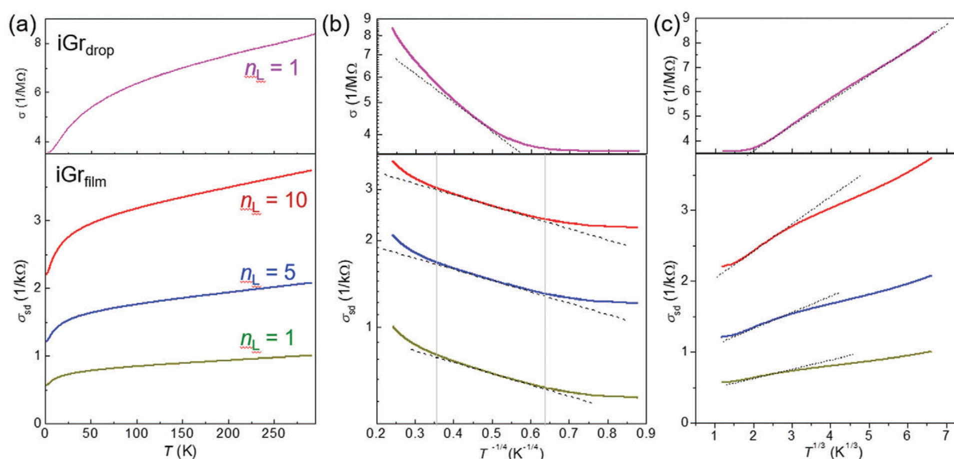

Figure 4. a) Temperature dependence of electrical conductivity at $B = 0$ for a single droplet, iGr_{drop}, and three film, iGr_{film}, devices with $n_L = 1$, 5, and 10. b) Fit of the data by the variable range hopping model. Dashed lines represent Equation (1). c) Fit of the data by the scaling model. Dashed lines represent Equation (2).

© 2024 The Authors. Small published by Wiley-VCH GmbH

16136829, 0, Downloaded from https://onlinelibrary.wiley.com/doi/10.1002/smll.202311416 by University Of Nottingham, Wiley Online Library on [05/03/2024]. See the Terms and Conditions (https://onlinelibrary.wiley.com/terms-and-conditions) on Wiley Online Library for rules of use; OA articles are governed by the applicable Creative Commons License

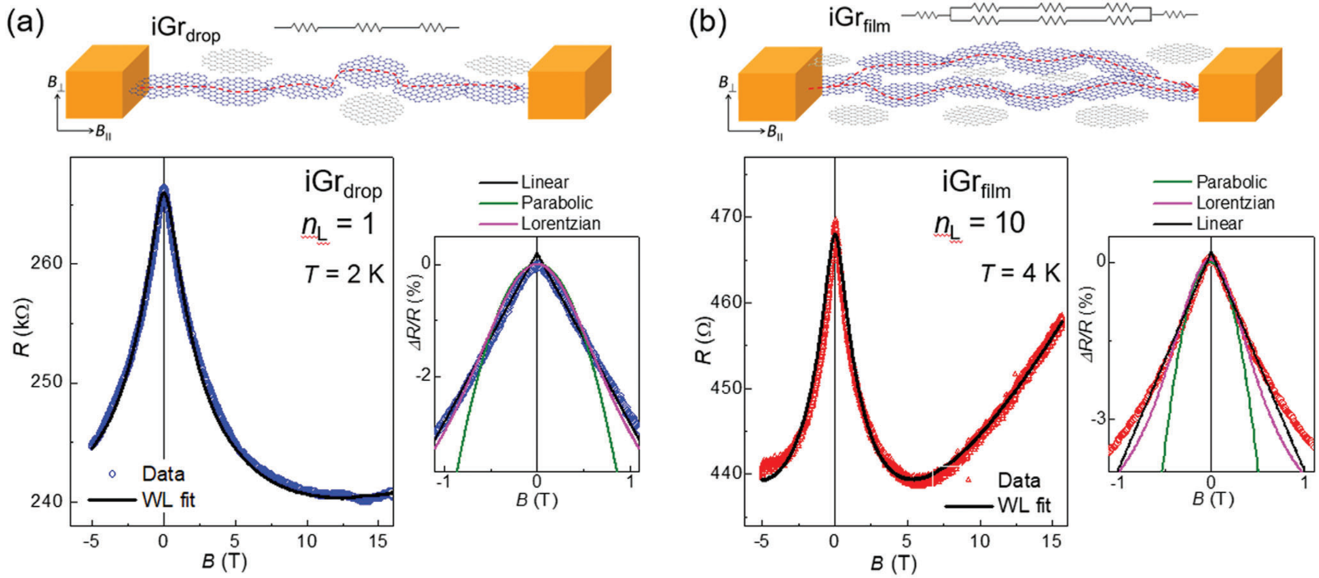

Figure 5. Resistance of a single droplet a) and $n_L = 10$ film b) iGr devices measured (data points) in magnetic fields -5 T $< B <$ 16 T and fitted by Equation (4) (solid black lines). Right insets: Relative magnetoresistances $\Delta R/R(B)$ at $B < 1$ T (data points) and their fits with linear (black line), parabolic (green line), and Lorentzian (magenta line) functions. Top insets: sketches of the current through the flake network in iGr$_{drop}$ (a) and iGr$_{film}$ (b) devices modeled as a network of series and parallel resistors.

$$\sigma \sim exp\left[\left(-\frac{T_0}{T}\right)^{1/4}\right] \tag{1}$$

and scaling model (Figure 4c):

$$\sigma \sim (1/T)^3 \tag{2}$$

2.2. Weak Localization in Low Magnetic Fields

iGr devices, particularly single-droplet devices, demonstrate electrical properties, such as triangular $\sigma(V_g)$ curve with minimum conductivity occuring at the V_g value for which the Fermi level passes through the Dirac point. When a small ($B < 5$ T) magnetic filed is applied normal to the graphene layer plane, the resistivity decreases with increasing B due to the weak localization effect[21,4,20] (**Figures** 2 and **5**). These observations are qualitatively similar to WL reported for single layer exfoliated,[6–8] SiC-grown,[22,23] CVD-grown[16,23] as well as multilayer iGr films films studied by other groups.[10,11] In this work, we observe WL in all printed devices including thick films ($n_L > 10$) with low mobility ($\mu < 100$ cm^2 V^{-1} s^{-1}) and at high magnetic fields, $B > 5$ T. This effect can be ascribed to the high ratio between the dephasing length L_φ responsible for the WL effect and the mean free path l_0 responsible for the orbital Landau level quantisation. This ratio can reach a value $L_\varphi/l_0 > 100$,[20] significantly reducing the characteristic magnetic field required for the observation of the WL effect. We observe saturation of the WL effect at magnetic field $B \approx 10$ T for iGr$_{drop}$ and $B \approx 4$ T for iGr$_{film}$ (Figure 2a,b), which are significantly higher than those reported for SLG ($B < 0.1$T).[8,6,23]

To explore this difference, we consider a 2D WL model of magnetoresistance developed for individual SLG flakes[4,23]:

$$\Delta\rho(B) = \frac{e^2\rho^2}{\pi h}\left[F\left(\frac{\tau_B^{-1}}{\tau_\varphi^{-1}}\right) - F\left(\frac{\tau_B^{-1}}{\tau_\varphi^{-1}+\tau_i^{-1}}\right) - 2F\left(\frac{\tau_B^{-1}}{\tau_\varphi^{-1}+\tau_*^{-1}}\right)\right] \tag{3}$$

where $F(x) = ln(x) + \psi(\frac{1}{2} + \frac{1}{x})$, ψ is the digamma function, τ_φ is the dephasing time due to inelastic scattering, τ_i is the elastic intervalley scattering time also associated with the edge scattering; τ_* is a scattering time relevant to a combination of different elastic intravalley scattering processes; $\tau_B^{-1} = 4eDB/\hbar$ where diffusion coefficient $D = \frac{v_F L_0}{2}$; Fermi velocity is $v_F = 106$ m s^{-1}; $L_0 = v_F\,\tau_{tr}$ is the mean free path where $\tau_{tr} = \frac{\mu m^*}{e}$ is the transport scattering time and electron effective mass $m^* \approx 0.08 m_e$ (at $V_g = 0$ and $p \approx 10^{13}$ cm^{-2}).[24,25]

Since iGr films consist of a random 3D network of individual 2D flakes, the flake arrangement needs to be accounted for, as it defines the electron trajectories. Random arrangement of individual flakes results in the random separation and overlap of neighboring flakes. As a result, the electron trajectories[14] can path through a chain of individual flakes (set of series resistors), which can branch to create local parallel paths (set of parallel resistors), see Figure 5a,b. With increasing iGr thickness, the contribution of parallel trajectories increases and dominates the charge transport. This explains the high resistance of iGr$_{drop}$ devices and decreasing resistance with increasing n_L for iGr$_{films}$. It also means that the device resistance, including its WL component, decreases with the increasing film thickness (Figure 5a,b). In order to include this effect into the classical model (3), we introduce an additional fitting parameter, N_{eff}, corresponding to an

 © 2024 The Authors. Small published by Wiley-VCH GmbH

16136829, 0, Downloaded from https://onlinelibrary.wiley.com/doi/10.1002/smll.202311416 by University Of Nottingham, Wiley Online Library on [05/03/2024]. See the Terms and Conditions (https://onlinelibrary.wiley.com/terms-and-conditions) on Wiley Online Library for rules of use; OA articles are governed by the applicable Creative Commons License

Table 1. Weak localization (WL) fitting parameters (Equation 4) for iGr_{drop} and iGr_{film} devices measured at $T = 4$ K.

Sample	Number of layers, n_L	ρ_{max} [Ω]	N_{gr}	τ_φ [ps]	τ_i [ps]	τ_* [ps]	L_φ [nm]
iGr_{drop}	1	266 000	0.1	5.0	7.5	0.15	14
iGr_{film}	1	1858	10	2.2	2.8	0.135	22.8
iGr_{film}	2	2135	7	2.38	2.26	0.115	23.7
iGr_{film}	5	866	20	2.12	2.4	0.158	22.4
iGr_{film}	10	468	31	2.3	2.3	0.16	23.3

effective number of parallel trajectories. Hence, we rewrite the Equation (3) as:

$$\Delta\rho_{iGr}(B) = N_{Gr}\frac{e^2\rho^2}{\pi h}\left[F\left(\frac{\tau_B^{-1}}{\tau_\varphi^{-1}}\right) - F\left(\frac{\tau_B^{-1}}{\tau_\varphi^{-1}+\tau_i^{-1}}\right) - 2F\left(\frac{\tau_B^{-1}}{\tau_\varphi^{-1}+\tau_*^{-1}}\right)\right] \quad (4)$$

Equation (4) provides a good fit for the experimental WL data for all our samples, both iGr_{drop} and iGr_{film} ($5 < N_{Gr} < 35$ for the iGr_{film} devices with the number of printed layers $1 < n_L < 10$) at the studied range of temperatures (Figure 5a,b; Section S3, Supporting Information). In iGr_{drop} devices the data are well fitted with $N_{Gr} < 1$ indicating the dominant contribution of the series, rather than parallel, inter-flake connections with significant junction resistance,[14] which decreases the iGr conductivity.

The dephasing (decoherence) length $L_\varphi = \sqrt{\tau_\varphi D}$ is ≈20 nm at $T < 5$ K for all the devices (**Table 1**) and decreases with increasing temperature (Section S3, Supporting Information). This value is similar to that previously reported for a large, multilayer iGr_{film} device ($L_\varphi \approx 15$ nm)[11] and is significantly smaller than values reported for SLG ($L_\varphi \approx 500$ nm),[23] suggesting much stronger confinement of the electron backscattering trajectories in iGr. In our samples, the lateral size of the graphene flakes is ≈50 nm (see Experimental Methods). Consequently, backscattering WL trajectories in our devices are likely to be fully localized within a single graphene flake at all of the studied temperatures

In all iGr devices we measure charge transport through randomly formed graphene networks. Our previous Monte Carlo modeling of electron trajectories in iGraphene transistors[12] demonstrated that while the formation of 3D networks of graphene flakes is random, it is statistically averaged over large number of flakes in our devices, hence we observe reproducible electrical properties in all studied samples. Localization of electron trajectories within a single flake can introduce large uncertainty in the modeling of iGr magnetoresistance. This uncertainty is due to the carrier mobility and scattering times used for the WL and quantizing magnetic field modeling being calculated using macroscopic resistances $R_{xx}(V_g)$ and $R_{xy}(B)$, which are affected by the resistances of the junctions between the flakes.[14] Carrier mobility of individual graphene flakes extracted from a graphene ink and/or of small devices consisting of few flakes can be significantly higher (≈400 cm^2 V^{-1} s^{-1})[26] compared to iGr_{film} mobility (≈10 cm^2 V^{-1} s^{-1}). High intra-flake mobility leads to the manifestation of quantum effects, such as weak localization and negative magnetoresistance. Also, high junction (inter-flake) resistance localizes electrons within individual flakes long enough for them to undergo the elastic, phase-coherent scattering, required for the WL. In this case, a maximum dephasing length is achieved for electron trajectories close to the edge of the flake. The shape of the $R_{xx}(B)$ WL effect reported for electron trajectories localized in small (≈1 μm^2) islands strongly depends on the island shape.[27,28] Conventional WL observed in macroscopic (sample size >> L_φ) 2D films results in a Lorentzian shape of $R(B)$ with $R(B) \approx -B^2$ near $B = 0$. However, for a small disk-shaped island (diameter $\approx L_\varphi$) this dependence is linear,[28] $R(B) \approx -B$, similar to that observed in our devices, where flake shape can be approximated to a disk with an aspect ratio of <2 (Figure 5a,b).[29] Interestingly, a reduced WL effect is also observed in our samples in magnetic fields applied parallel to the sample surface (dashed lines in Figure 1b,c); this is unlike SLG where WL is suppressed due to enhanced spin scattering mediated by impurities.[22] We attribute the observation of WL in iGr in parallel *B*-field to the random orientation of individual flakes within the network (Section S4, Supporting Information). We note, that since our experimental results for devices produced with different number of printed layers are fitted with comparable values of all scattering times (Equations (3) and (4)) and their magnetoresistance data (Figure 2c) are similar, we attribute the observation of weak localisation (WL) in iGraphene to the dephasing length, $L\varphi \approx 20$ nm (Table 1), which is significantly lower than that estimated for single layer graphene ($L\varphi \sim 500$ nm[23]).

2.3. Landau Quantisation and Negative Magnetoresistance in High Magnetic Fileds

At low temperatures ($T = 4.2$ K) the inkjet-printed graphene films exhibit monotonic MR lineshapes for magnetic fileds up to $B = 56$ T with no signature of Shubnikov- de Haas oscillations (Figure 1b,c), which we ascribe to the low macroscopic carrier mobility $\mu \approx 10$ cm^2 V^{-1} s^{-1}. In the iGr devices, the low mobility is ascribed to the resistance at the flake-to-flake junctions and inter-flake scattering. We suggest that these processes can be less significant in small droplet devices because of the different current paths (Figure 5 insets). Also the role of inter-flake junctions can be significantly reduced by applied high magnetic fields, which confine electron trajectories within individual flakes.

The criterion required for the Landau quantisation, $\mu B > 1$, cannot be achieved in these devices ($\mu B > 1$ only at $B > 1000$ T). In high magnetic fields ($B > 20$ T), WL is suppressed by the field-induced dephasing of the electron wavefunction. At the same time, electron trajectories may still be confined within individual flakes maintaining large microcopic, intra-flake mobility. This leads to the formation of Landau levels and skipping orbits near the flake edge. As the orbital degeneracy of the Landau

© 2024 The Authors. Small published by Wiley-VCH GmbH

16136829, 0, Downloaded from https://onlinelibrary.wiley.com/doi/10.1002/smll.202311416 by University Of Nottingham, Wiley Online Library on [05/03/2024]. See the Terms and Conditions (https://onlinelibrary.wiley.com/terms-and-conditions) on Wiley Online Library for rules of use; OA articles are governed by the applicable Creative Commons License

16136829, 0, Downloaded from https://onlinelibrary.wiley.com/doi/10.1002/smll.202311416 by University Of Nottingham, Wiley Online Library on [05/03/2024]. See the Terms and Conditions (https://onlinelibrary.wiley.com/terms-and-conditions) on Wiley Online Library for rules of use; OA articles are governed by the applicable Creative Commons License

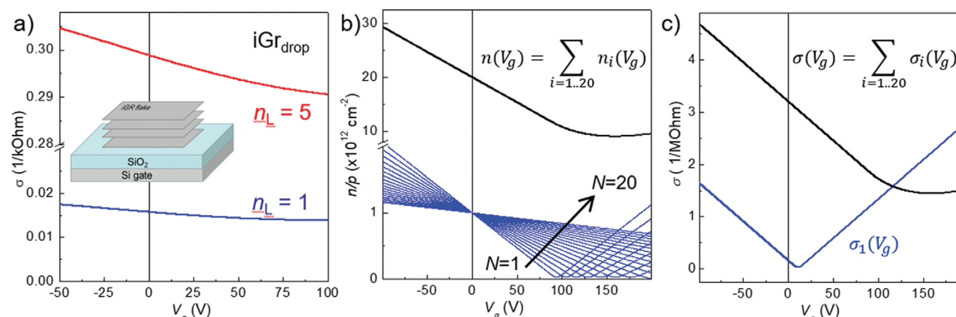

Figure 6. a) Gate voltage dependence of the conductivity of a single iGr$_{drop}$ and 5 droplet devices at $B = 0$ and $T = 300$ K. Inset: Schematics of the used parallel iGr flake model b) Blue curves: modelling of the carrier concentration in 20 parallel iGr flakes with the layer screening factor SF = 0.9, $p_0 = 10^{12}$ cm^{-2} and $\mu = 10$ cm^2/Vs (Section S5, Supporting Information). Black curve: carrier concertation as a function of applied V_g. c) Modeling of the conductivity of iGr assuming single layer graphene (blue line) and 20 paralel flakes (black line).

levels is proportional to the applied magnetic field, the increased density of states at the Landau level energies favors flake-to-flake transport leading to negative MR observed in iGr$_{drop}$ devices (Figure 1b). We suppose that for very high magnetic fields, only the lowest Landau levels in different flakes are partially populated and roughly aligned in energy (e.g., within their typical broadening energy range). This effect is not observed in parallel magnetic fields (Figure 1b) as well as in thick iGr$_{film}$ samples, where charge transport is dominated by parallel trajectories and can be described using classical positive parabolic MR (Figure 1c). Note, that all samples studied here were fabricated using the same ink and deposition process, and have identical composition. Hence, the observed negative MR, observed only in iGr$_{drop}$ devices, cannot be explained by spin-dependent scattering on defects and impurities.[30–32] Consequently, our printed devices enable ensemble averaging of quantum interference phenomena within a single device. Our work therefore highlights the potential of printed devices as testbeds for the experimental study of statistical aspects of quantum transport.

2.4. Effect of the Applied Electric Field on Charge Transport in iGr

The triangular shape of $\sigma(V_g)$ for a graphene FET is evidence of the Dirac cone energy dispersion. In iGr devices, intra-flake transport and electric-field-controlled inter-flake transport[12,33] can influence the shape of $\sigma(V_g)$, leading to the observation of the minimum of $\sigma(V_g)$ at $V_g \approx 0$.[12,33] Our iGr$_{drop}$ devices demonstrate $\sigma(V_g)$ (**Figure 6a**) similar to that of CVD graphene,[15] where a conductivity minimum is observed at $V_g > 80$ V, corresponding to a high level of p-type doping, $p \approx 10^{13}$ cm^2 V^{-1} s^{-1} and low carrier mobility <100 cm^2 V^{-1} s^{-1}. In contrast, iGr$_{film}$ devices demonstrate very weak or unmeasurable gate voltage dependence of the conductivity (Section S2, Supporting Information). For these graphene inks, the thickness of single printed layer is ≈15 nm,[10,11,34,35] hence gate-induced electric field can penetrate only a skin layer of the film due to graphene screening of the applied electric field.[36] Therefore no V_g dependence of the conductivity is observed.

A shift of $\sigma(V_g)$ observed in iGr$_{film}$ devices (e.g., for iGr$_{film}$ with $n_L = 5$, Figure 3a) is indicative of the change of carrier concentration, suggesting weak electric field screening in iGr. A qualitative model that assumes charge transport through a series of vertically oriented SLG layers and an electric field screening factor $SF = 0.9$ (90% of the applied electric field propagates to the next layer) is used to describe the experimental results (Figure 6a,b). The increasing number of vertically oriented graphene flakes affects the minimum conductivity, the carrier concentration and field effect mobility by shifting the V_g relevant to the Dirac point toward higher voltages and changing the slope of $\sigma(V_g)$ (Figure 6c). This dependence also results in a large error in carrier mobility calculated using a three-point $R_{xx}(V_g)$ fit[37] (Section S2, Supporting Information):

$$\mu = \frac{4}{e\delta n\rho_{max}} \tag{5}$$

where ρ_{max} is the peak resistivity at the neutrality point, and δn is an uncertainty in the bipolar carrier density calculated from the full width at half maximum (FWHM) of the resistivity peak expressed in terms of carrier density.[37] The difference between the field-effect mobility calculated using the linearization model[9] and a three-point fit[37] can be used as a qualitative indicator that electrons in the GFET flow through several parallel trajectories.

In contrast to SLG,[6,8] applied gate voltage has very little effect on the WL in iGr$_{drop}$ devices (Figure 3b,c), as the electron trajectories are confined by the edges of individual flakes. However, applied V_g affects the onset of negative MR, which is shifted toward higher magnetic fields ($B > 30$ T) in low and negative V_g (with higher hole concentrations, Figure 3c), as higher magnetic field is required to reach the same Landau level. Interestingly, the slope of negative MR observed for all applied V_g at $B > 35$ T is comparable (Figure 3c), could be due to the fact that only the lowest Landau level is populated in all flakes, resulting in the V_g independent density of states.

2.5. Temperature Dependence of Charge Transport

Inter-flake conductivity in iGr$_{film}$ is attributed to different charge hopping mechanisms.[11,14] Temperature dependences of conductivity, $\sigma(T)$, for our iGr$_{drop}$ and iGr$_{film}$ devices (Figure 4) was fitted using two different models: 3D VRH conductivity (Equation (1)) and scaling model (Equation (2)). The 3D VRH explains

© 2024 The Authors. Small published by Wiley-VCH GmbH

Table 2. Analysis of the experimental data for iGr devices.

Experiment	Observed Effect	Device	Classical	Quan-tum
Electric field	SLG-like shape of $\sigma(V_g)$	iGr_{drop}		X
	$\sigma(V_g) = const$	iGr_{film}	X	
Temperature	Hopping conductivity[20] $\sigma \approx exp[(-\frac{T_0}{T})^{1/4}]$	iGr_{film}	X	
	Scaling model of conductivity[20] $\sigma \approx (1/T)^3$	iGr_{drop}	X	X
Magnetic field	WL in magnetic field $\sigma(B)$	All		X
	Negative magnetoresistance	iGr_{drop}		X
	Positive parabolic magnetoresistance	iGr_{film}	X	

$\sigma(T)$ of the iGr_{film} devices with $n_L = 1$ to 10 at temperature range 6 K < T < 60 K (Figure 4b). However, at the lowest and highest accessible temperatures, the model deviates from the experimental data suggesting the contributions from weak localization and phonon scattering. In contrast, $\sigma(T)$ of a single iGr_{drop} device demonstrates $\sigma \approx T^{1/3}$ behavior (Figure 4c), typical for 2D conductors and is strongly dependent on the device size.[20,21,38] The temperature-dependent studies further confirm that conductivity of the thin iGr_{drop} devices is mediated by the 2D electron trajectories confined within individual graphene flakes, while transport in thick iGr_{film} devices can be described using classical VRH and parabolic MR models.

In summary, our temperature dependent magnetic and electric field studies (**Table 2**) demonstrate that the charge transport in iGr devices is strongly affected by the flake orientation and network thickness, with iGr_{film} devices demonstrating 3D hopping conductivity with dominating percolation transport, while iGr_{drop} devices having metallic type conductivity with strong quantum correction to the Drude transport.

3. Conclusion

In this paper we presented an experimental study of electron transport in droplet (created by one or several printed droplets) and film (created by one or several printed layers) iGr devices in high (B < 60 T) magnetic fields, gate-induced electric fields, and wide (1.5 K < T < 400 K) temperature range. The data has been analyzed using a number of classical and quantum transport models to determine relevant processes and mechanisms in different iGr devices. Our analysis demonstrates that neither pure quantum nor pure classical modeling can be applied to iGr. However, under certain conditions, such as those achieved in the droplet samples, iGr behaves mostly as a quantum material similar to a single layer graphene with high doping level (~10^{13} cm^{-2}) and very low mobility (~10 cm^2 V^{-1} s^{-1}). We also demonstrated that the interplay of quantum and classical effects in this material defines the carrier transport and both effects should be accounted for in modeling of iGr devices. Confinement of electron trajectories within individual graphene flakes and high intra-flake mobility is suggested for the modeling of high magnetic field carrier transport and quantum effects in iGr. This results underpin fundamental understanding of the behavior of graphene networks, and will inform development of the next generation of devices utilizing graphene networks, including additively manufactured and 3D-printed devices.

4. Experimental Section

Materials: The graphene-polymer ink was purchased from Sigma-Aldrich (product number: 793663) and consisted of liquid exfoliated graphene flakes (average area of 2590 nm^2, average size ≈50 nm)[34] encapsulated in ethyl cellulose (EC) dispersed into an 85:15 mixture of cyclohexanone/terpineol to achieve suitable rheological properties for inkjet printing. At a concentration of 2.4 wt% solids, this ink had a density of 9.665 g cm^{-3}, surface tension of 33 mN m^{-1} and viscosity of 11.3 mPa·s at room temperature. The hBN-polymer ink was also purchased from Sigma-Aldrich (product number 901410) with 5.4% wt EC-hBN composite solids dispersed in the same solvents described above. The AgNP ink was purchased from Advanced Nano Products (product ID: SilverJet DGP-40LT-15C) and consisted of 38.85 wt% of silver nanoparticles dispersed in triethylene glycol monomethyl ether (TGME) and other dispersants.

Inkjet Printing of Film iGr Devices: Graphene ink was deposited on sapphire or Si/SiO_2 (300 nm of SiO_2) substrate using a drop-on-demand (DoD) piezo driven inkjet printer Fujifilm Diamatix DMP-2800 and a 10 pL drop volume cartridge with nozzles of a = 21.5 µm, Z = 7.3. A drop spacing of 20 µm was used. A pause of 30 s between layers was used to allow evaporation of the solvents in order to achieve improved surface morphology and geometrical precision. The films were then annealed for two hours in a vacuum oven under 1 mbar vacuum at annealing temperature of 250 °C. To ensure precise printing geometry, the silver electrodes were printed with 30 µm drop spacing for 1 layer on a heated stage at 90 °C and then annealed under 1 mbar vacuum for 30 min for curing. Film devices were produced with the size > 500 µm using 1 to 20 printed layers. Contacts to the sample holder are made using DuPont 4929N silver paste an gold wires.

Inkjet Printing of Droplet iGr Devices: Individual droplets of the same graphene ink were deposited onto Si/SiO_2 substrate with Ti/Au electrodes using a drop-on-demand (DoD) piezo driven inkjet printer Fujifilm Diamatix DMP-2800 and a 10 pL drop volume cartridge with nozzles of a = 21.5 µm, Z = 7.3. Diameter of a dried droplet is ≈50 µm, distance between the Au electrodes 5–20 µm. For multi-droplet devices a pause of 30 s was used between the deposition of individual droplets to allow evaporation of the solvents. The samples were annealed in a vacuum oven (1 mbar) at annealing temperature of 250 °C for 2 h.

Studies in Low Magnetic Fields $B \leq 16$ T: Experimental measurements in constant and slow-changing magnetic fields were performed in a closed-cycle 16 T superconducting solenoid system (Cryogenics Ltd), which includes a cryostat temperature control inset (1.5 K < T < 400 K). For magnetic field-dependent studies, a field sweep rate of ≈0.005 T s^{-1} was used. DC voltage-current dependences were measured using

© 2024 The Authors. Small published by Wiley-VCH GmbH

16136829, 0, Downloaded from https://onlinelibrary.wiley.com/doi/10.1002/smll.202311416 by University Of Nottingham, Wiley Online Library on [05/03/2024]. See the Terms and Conditions (https://onlinelibrary.wiley.com/terms-and-conditions) on Wiley Online Library for rules of use; OA articles are governed by the applicable Creative Commons License

16136829, 0, Downloaded from https://onlinelibrary.wiley.com/doi/10.1002/smll.202311416 by University Of Nottingham, Wiley Online Library on [05/03/2024]. See the Terms and Conditions (https://onlinelibrary.wiley.com/terms-and-conditions) on Wiley Online Library for rules of use; OA articles are governed by the applicable Creative Commons License

Keithley-2400 SourceMeter and Keithley-2010 multimeter units. All the studied devices demonstrated linear dependence of current on source-drain voltage, V_{sd}, and negligible (< 10 Ω) contact resistance.

Studies in High Magnetic Fields $B \leq 60$ T: Pulsed magnetic field measurements were performed up to $B \leq 60$ T. The pulsed magnetic fields were created by discharging a capacitor through a liquid nitrogen-cooled resistive coil in a short time (300 ms for the total pulsed field duration). The sample was placed in a helium cooled cryostat and measured in the temperature range 4 K < T < 300 K. A constant DC V_{sd} and V_g voltages were applied using Keithley-2400 SourceMeters. The values of longitudinal and transverse voltages were amplified by Stanford SR560 low noise amplifiers and measured using a fast multichannel PXI acquisition card (National Instruments). For the measurements of the longitudinal and transverse voltages in pulsed magnetic fields. A parasitic voltage proportional to dB/dt was superimposed to the signal. The value of dB/dt correction was obtained through the measurement on a separated channel of the voltage across a copper wire winding located around the sample holder, which was used to compensate parasitic contribution. The correction was assessed by checking that the field up and field down sweep voltage traces with different dB/dt superimpose. See Section S6 (Supporting Information) for details.

Statistical Analysis: All measurements were performed with three independent repeats, where applicable, and the data are reported as averadge value and standard deviation.

Supporting Information

Supporting Information is available from the Wiley Online Library or from the author.

Acknowledgements

N.D.C. and F.W. contributed equally to this work. The authors acknowledge support from the Engineering and Physical Sciences Research Council [grant number EP/P031684/1]; Engineering and Physical Sciences Research Council via its membership to the European Magnetic Field Laboratory [grant number EP/N01085X/1 and NS/A000060/1]; and the DSTL. University of Nottingham Propulsion Futures Beacon for funding toward this research; The high magnetic field measurements were performed at LNCMI-Toulouse under EMFL proposal TSC09-221.

Conflict of Interest

The authors declare no conflict of interest.

Data Availability Statement

The data that support the findings of this study are available from the corresponding author upon reasonable request.

Keywords

high magnetic field, jet printed graphene, Landau levels, weak localisation

Received: December 7, 2023
Revised: January 31, 2024
Published online:

[1] A. K. Geim, K. S. Novoselov, *Nat. Mater.* **2007**, *6*, 183.
[2] K. S. Novoselov, A. K. Geim, S. V. Morozov, D. Jiang, Y. Zhang, S. V. Dubonos, I. V. Grigorieva, A. A. Firsov, *Science* **2004**, *306*, 666.
[3] K. S. Novoselov, Z. Jiang, Y. Zhang, S. V. Morozov, H. L. Stormer, U. Zeitler, J. C. Maan, G. S. Boebinger, P. Kim, A. K. Geim, *Science* **2007**, *315*, 1379.
[4] E. McCann, K. Kechedzhi, V. I. Fal'ko, H. Suzuura, T. Ando, B. L. Altshuler, *Phys. Rev. Lett.* **2006**, *97*, 146805.
[5] S. Lara-Avila, S. Kubatkin, O. Kashuba, J. A. Folk, S. Luscher, R. Yakimova, T. J. B. M. Janssen, A. Tzalenchuk, V. Fal'ko, *Phys. Rev. Lett.* **2015**, *115*, 106602.
[6] F. V. Tikhonenko, D. W. Horsell, R. V. Gorbachev, A. K. Savchenko, *Phys. Rev. Lett.* **2008**, *100*, 056802.
[7] S. V. Morozov, K. S. Novoselov, M. I. Katsnelson, F. Schedin, L. A. Ponomarenko, D. Jiang, A. K. Geim, *Phys. Rev. Lett.* **2006**, *97*, 016801.
[8] F. V. Tikhonenko, A. A. Kozikov, A. K. Savchenko, R. V. Gorbachev, *Phys. Rev. Lett.* **2009**, *103*, 226801.
[9] S. V. Morozov, K. S. Novoselov, M. I. Katsnelson, F. Schedin, D. C. Elias, J. A. Jaszczak, A. K. Geim, *Phys. Rev. Lett.* **2008**, *100*, 016602.
[10] G. Calabrese, L. Pimpolari, S. Conti, F. Mavier, S. Majee, R. Worsley, Z. H. Wang, F. Pieri, G. Basso, G. Pennelli, K. Parvez, D. Brooks, M. Macucci, G. Iannaccone, K. S. Novoselov, C. Casiraghi, G. Fiori, *Nanoscale* **2020**, *12*, 6708.
[11] E. Piatti, A. Arbab, F. Galanti, T. Carey, L. Anzi, D. Spurling, A. Roy, A. Zhussupbekova, K. A. Pater, J. M. Kim, D. Daghero, R. Sordan, V. Nicolosi, R. S. Gonnelli, F. Torrisi, *Nat. Electron.* **2021**, *4*, 893.
[12] F. R. Wang, J. H. Gosling, G. F. Trindade, G. A. Rance, O. Makarovsky, N. D. Cottam, Z. Kudrynskyi, A. G. Balanov, M. T. Greenaway, R. D. Wildman, R. Hague, C. Tuck, T. M. Fromhold, L. Turyanska, *Adv. Funct. Mater.* **2021**, *31*, 2007478.
[13] A. Bastola, Yi. He, J. Im, G. Rivers, F. Wang, R. Worsley, J. S. Austin, O. Nelson-Dummett, R. D. Wildman, R. Haugue, C. J. Tuck, L. Turyanska, *Mater. Today Electron.* **2023**, *6*, 100058.
[14] S. Barwich, J. Medeiros de Araújo, A. Rafferty, C. Gomes da Rocha, M. S. Ferreira, J. N. Coleman, *Carbon* **2021**, *171*, 306.
[15] R. Negishi, Y. Ohno, K. Maehashi, K. Matsumoto, Y. Kobayashi, *Jpn. J. Appl. Phys.* **2012**, *51*, 06FD03.
[16] L. A. Jauregui, H. Cao, W. Wu, Q. Yu, Y. P. Chen, *Solid State Commun.* **2011**, *151*, 1100.
[17] Y. Hernandez, V. Nicolosi, M. Lotya, F. M. Blighe, Z. Sun, S. De, I. T. McGovern, B. Holland, M. Byrne, Y. K. Gun'Ko, J. J. Boland, P. Niraj, G. Duesberg, S. Krishnamurthy, R. Goodhue, J. Hutchison, V. Scardaci, A. C. Ferrari, J. N. Coleman, *Nat. Nanotechnol.* **2008**, *3*, 563.
[18] N. F. Mott, E. A. Davis, *Electronic Processes in Non-Crystalline Materials*, Clarendon Press, Oxford, **1971**, p. 437.
[19] N. F. Mott, *Metal-Insulator Transitions*, 2nd ed., Taylor & Francis, London; New York, **1990**, p. 286.
[20] V. F. Gantmakher, *Electrons and Disorder in Solids*, Clarendon Press, Oxford University Press, Oxford; New York, **2005**, p. 225.
[21] P. A. Lee, T. V. Ramakrishnan, *Rev. Mod. Phys.* **1985**, *57*, 287.
[22] S. Lara-Avila, S. Kubatkin, O. Kashuba, J. A. Folk, S. Luscher, R. Yakimova, T. J. Janssen, A. Tzalenchuk, V. Fal'ko, *Phys. Rev. Lett.* **2015**, *115*, 106602.
[23] A. M. R. Baker, J. A. Alexander-Webber, T. Altebaeumer, T. J. B. M. Janssen, A. Tzalenchuk, S. Lara-Avila, S. Kubatkin, R. Yakimova, C. T. Lin, L. J. Li, R. J. Nicholas, *Phys. Rev. B* **2012**, *86*, 235441.
[24] K. S. Novoselov, A. K. Geim, S. V. Morozov, D. Jiang, M. I. Katsnelson, I. V. Grigorieva, S. V. Dubonos, A. A. Firsov, *Nature* **2005**, *438*, 197.
[25] O. Makarovsky, L. Turyanska, N. Mori, M. Greenaway, L. Eaves, A. Patané, M. Fromhold, S. Lara-Avila, S. Kubatkin, R. Yakimova, *2D Mater.* **2017**, *4*, 031001.
[26] S. Wang, P. K. Ang, Z. Wang, A. L. Tang, J. T. Thong, K. P. Loh, *Nano Lett.* **2010**, *10*, 92.

© 2024 The Authors. Small published by Wiley-VCH GmbH

[27] H. U. Baranger, R. A. Jalabert, A. D. Stone, *Phys. Rev. Lett.* **1993**, *70*, 3876.
[28] A. M. Chang, H. U. Baranger, L. N. Pfeiffer, K. W. West, *Phys. Rev. Lett.* **1994**, *73*, 2111.
[29] H. Chacham, J. C. C. Santos, F. G. Pacheco, D. L. Silva, R. M. Martins, J. P. Del'Boccio, E. M. Soares, R. Altoé, C. A. Furtado, F. Plentz, B. R. A. Neves, L. G. Cançado, *ACS Appl. Nano Mater.* **2020**, *3*, 12095.
[30] R. P. Khosla, J. R. Fischer, *Am. Phys. Soc.* **1970**, *15*, 316.
[31] M. Rein, N. Richter, K. Parvez, X. Feng, H. Sachdev, M. Klaui, K. Mullen, *ACS Nano* **2015**, *9*, 1360.
[32] J. H. Chen, L. Li, W. G. Cullen, E. D. Williams, M. S. Fuhrer, *Nat. Phys.* **2011**, *7*, 535.
[33] C. J. Adkins, *Mater. Res. Soc. Symp. P* **1990**, *195*, 223.
[34] E. B. Secor, P. L. Prabhumirashi, K. Puntambekar, M. L. Geier, M. C. Hersam, *J. Phys. Chem. Lett.* **2013**, *4*, 1347.
[35] E. Jabari, F. Ahmed, F. Liravi, E. B. Secor, L. Lin, E. Toyserkani, *2D Mater.* **2019**, *6*, 042004.
[36] H. Rokni, W. Lu, *Sci. Rep.* **2017**, *7*, 42821.
[37] J. H. Gosling, S. V. Morozov, E. E. Vdovin, M. T. Greenaway, Y. N. Khanin, Z. Kudrynskyi, A. Patane, L. Eaves, L. Turyanska, T. M. Fromhold, O. Makarovsky, *Nanotechnology* **2023**, *34*, 125702.
[38] I. Shlimak, M. Kaveh, R. Ussyshkin, V. Ginodman, L. Resnick, *Phys. Rev. Lett.* **1996**, *77*, 1103.

© 2024 The Authors. Small published by Wiley-VCH GmbH

16136829, 0, Downloaded from https://onlinelibrary.wiley.com/doi/10.1002/smll.202311416 by University Of Nottingham, Wiley Online Library on [05/03/2024]. See the Terms and Conditions (https://onlinelibrary.wiley.com/terms-and-conditions) on Wiley Online Library for rules of use; OA articles are governed by the applicable Creative Commons License